Key Points:
- The Global-scale Observations of Limb and Disk (GOLD) instrument observes the Earth in the Far-Ultraviolet (FUV) from a geostationary orbit
- GLOW adequately calculates the FUV brightness for various local times, latitudes, solar forcing, and lower atmospheric forcing
- GLOW calculations indicate the oxygen brightness varies by ±45 R and the effective temperature varies by more than 80 K due to tides

Correspondence to:
K. R. Greer,
katelynn.greer@lasp.colorado.edu

Variations of Lower Thermospheric FUV Emissions Based on GOLD Observations and GLOW Modeling

K. R. Greer[1] [ID], Richard Eastes[1] [ID], Stan Solomon[2] [ID], William McClintock[1] [ID], Alan Burns[2] [ID], and David Rusch[1]

[1]University of Colorado Boulder-LASP, Boulder, CO, USA, [2]National Center for Atmospheric Research-HAO, Boulder, CO, USA

Abstract Here we compare the global-scale morphology of Earth's the Far-Ultraviolet (FUV) emissions observed by NASA's Global-scale Observations of Limb and Disk (GOLD) mission to those modeled using the Global Airglow (GLOW) code with atmospheric parameters provided by Thermosphere-Ionosphere-Electrodynamics General Circulation Model (TIEGCM). The O ^{5}S oxygen (135.6 nm) and N_2 Lyman-Birge-Hopfield (LBH) emissions are observed over the Western hemisphere every 30 min by the GOLD instrument. The FUV brightness of the thermosphere-ionosphere is expected to vary in systemic ways with respect to geophysical parameters, solar energy input from above, and terrestrial weather input from below. In this paper we examine the O ^{5}S oxygen emission and the N_2 LBH emission brightnesses with local time, latitude, season, tides, geomagnetic activity, and solar activity based on GOLD observations and GLOW modeling. Early GOLD observations indicate that the model effectively reproduces the brightness variations with local time and latitude but is biased low in magnitude. However, the TIEGCM is unable to accurately represent the extraordinary nighttime equatorial ionization anomaly observed by GOLD. It is also expected from these results that the signal from geomagnetic storms may obscure tidal signals.

Plain Language Summary In January 2018, a FUV instrument, the Global-scale Observations of Limb and Disk (GOLD), was launched as a NASA mission of opportunity aboard a geostationary satellite and scientific operations began in October of 2018. GOLD views the entire disk of the Earth every 30 min, allowing the separation of geophysical variability in both space and time. This allows an unprecedented test of global models. Here, we model the Earth's upper atmosphere using the Thermosphere-Ionosphere-Electrodynamics General Circulation Model (TIEGCM), which produces temperature and the densities of the major chemical components of the neutral atmosphere, ionized plasma densities, and neutral air temperatures. These atmospheric temperatures and densities are used to calculate the Earth's upper atmosphere emissions in the Far-Ultraviolet (FUV) with the Global Airglow (GLOW) model. The calculated emission rates are then used to compute the expected FUV signals as observed from geostationary orbit. In this paper, we show how the FUV brightness varies with local time, season, atmospheric activity, and solar activity. Of particular interest is that the GLOW model excels at producing FUV brightnesses that match the local time and latitude trends of the daytime observations; however, the model fails to adequately portray the extraordinary nighttime phenomena observed by GOLD.

1. Introduction

Characterization of Earth's ionosphere, and the thermosphere to which it is coupled, is critical for communications and navigational technologies (Knipp et al., 2016). The lower and middle thermosphere and ionosphere (approximately 100 to 400 km) are influenced from both above (e.g., solar inputs) and below (e.g., atmospheric waves and tides). Due to these influences, this region experiences a wide range of dynamic variability, on a large spectrum of spatial scales and temporal scales.

Remote sensing is one of the most practical ways to gain information about the temperature and composition over the necessary spatial and temporal scales required for interpreting the dynamics that impact modern communications and navigational technologies. The Far-Ultraviolet (FUV), spanning approximately 110–180 nm, is an ideal range to study the weather of this region. When the Earth is viewed from space, the Earth's lower atmosphere is opaque in the FUV, providing a dark background for FUV variations in

the thermosphere. Also, the FUV contains spectral signatures of constituents of the lower thermosphere (O and N_2), allowing the derivation of temperature and composition.

On the dayside, at 135.6 nm, an atomic oxygen emission line is created by photoelectron impact excitation and radiative recombination of O^+, as well as the photoelectron impact excitation of molecular nitrogen generates the LBH emissions. On the nightside, FUV captures the emissions from the F-region recombination of O^+. The solar spectrum that produces the FUV emissions exhibits significant geophysical variability (Paxton et al., 2003) to which the dayglow and nightglow are sensitive (Conway et al., 1988; Strickland et al., 1995).

The technology for observing the Earth in the FUV has been maturing for some five decades. The OGO-4 ultraviolet spectrometer measured nightglow at tropical latitudes, including the 1304- and 1356-A lines of atomic oxygen (Barth & Schaffner, 1970); additional observations of the aurora were also made in the FUV (Chubb & Hicks, 1970). A far-ultraviolet camera/spectrograph experiment was operated on the lunar surface during the Apollo 16 mission; this gave the spatial distributions and relative intensities of emissions from atomic hydrogen, atomic oxygen, molecular nitrogen, and other species—Some observed spectrographically for the first time (Carruthers & Page, 1972). Nadir views of the airglow and aurora were made on the polar orbiting S3-4 satellite in the late 1970s (Huffman et al., 1980). Some of the first global images were made by Spin-scan Auroral Imaging (SAI) on DE1 (Frank, 1998). Observations at 3.5A resolution using an Fastie-Ebert monochromator were made from a sounding rocket in the 1980s (Eastes et al., 1985). The technology was pushed forward with the launch of the V5 ultraviolet auroral imager aboard the Viking spacecraft in 1986, which had improved spatial and temporal resolution (Anger et al., 1987). Additional improvements in spatial and temporal resolution were made with the Freja program of the 1990s (Murphree et al., 1994) and the Ultraviolet Imager for the Global Geospace Sciences (Torr et al., 1995) of the International Solar-Terrestrial Physics program. At the same time, modeling demonstrated the spatial extent and short-term temporal stability of brightness perturbations in the FUV (Nicholas et al., 1997). Additionally, new models of the emissions in the FUV by Earth's atmosphere by the dominant constituents (Eastes, 2000) were developed. A FUV instrument was flown aboard the NASA Imager for Magnetopause to Aurora Global Exploration (IMAGE) mission that could image Doppler shifted H Lyman alpha, OI 1356-A, and the N_2 LBH emissions (Mende et al., 2000). The Special Sensor Ultraviolet Spectrographic Imager (SSUSI) and the Global Ultraviolet Imager (GUVI) brought advances in the use of a full image cubes (two-dimensional detectors and full FUV wavelength coverage) and large instantaneous FOV (Paxton et al., 2003). Using a forward model, GUVI is able to derive O, N_2, and O_2 on the limb (Christensen et al., 2003; Meier et al., 2015; Strickland et al., 2004). On the disk, GUVI derives O/N_2 using the algorithm described by Strickland et al. (1995). Current FUV sensor includes the SSUSI-Lite sensor (Paxton et al., 2017), the Global-scale Observations of Limb and Disk (GOLD) (Eastes et al., 2017) instrument launched in January 2018, and the Ionospheric Connections Explorer (ICON) FUV instrument (Mende et al., 2017) launched in 2019.

The GOLD instrument was launched aboard the SES-14 communication satellite on 25 January 2018 and began its observational operations in October of 2018. The mission is located in a geostationary orbit over 47.5°W longitude. GOLD is a far-ultraviolet (FUV) imaging spectrograph. From the radiances at different spectral bands, thermospheric temperature and composition can be derived. The equatorial ionospheric structure and plasma density are also provided (Eastes et al., 2017). Here we describe the FUV emissions predicted to be observed by GOLD and some actual GOLD observations for comparison. In this paper, we use the Global Airglow (GLOW) model to calculate the 135.6 nm and LBH emissions which are observed in thermosphere by the GOLD mission. The atmosphere itself is modeled by the TIEGCM. GOLD has a unique vantage point from geostationary orbit that will be able to separate the spectrums of spatial and temporal variability.

2. Methodology

GOLD is an imaging spectrometer, and the returned image cubes (one spectral and two spatial dimensions) contain information about the geographic position, time, and wavelength of atmospheric emissions. Two models are used in this study along with early observations from GOLD. The Global Airglow (GLOW) model calculates the Far-Ultraviolet and other atmospheric emission features for a given atmosphere (Solomon, 2017). The upper atmosphere used as input to GLOW is modeled by the TIEGCM.
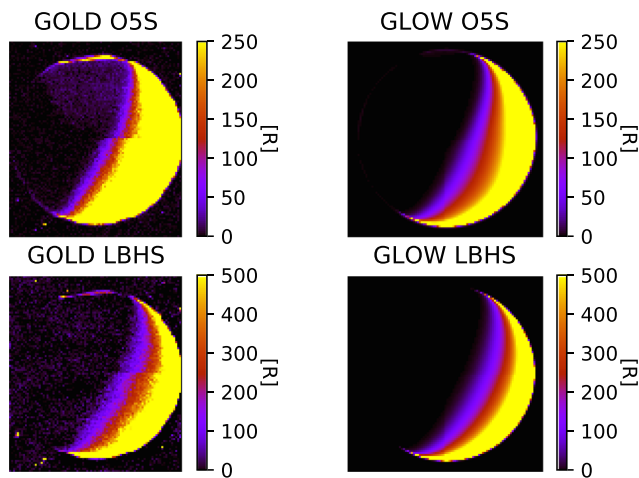
Figure 1. Panels display GOLD observations and TIEGCM/GLOW modeling for 15 December 2018 at 9 UT for both the 135.6 nm oxygen emission (O ^{5}S) and the LBH short bands emissions. F10.7 was 72 SFU, and Kp index was 0. The color scale is in Rayleighs and saturates at 250 R (500 R) in the O ^{5}S (LBH) emission.

2.1. TIEGCM

The Thermosphere-Ionosphere-Electrodynamics General Circulation Model (TIEGCM) is a self-consistent, numerical model of Earth's upper atmosphere (Richmond et al., 1992; Qian et al., 2014). Here we use the TIEGCM-ICON version at a 2.5° resolution. This version of TIEGCM was developed in support of the ICON mission and is described more thoroughly by Maute (2017) and Greer et al. (2018).

2.2. GLOW

The Global Airglow (GLOW) model calculates various FUV emissions of the upper atmosphere (Solomon, 2017). Of particular interest here are the Lyman-Birge-Hopfield (LBH) bands of molecular nitrogen and the atomic doublet at 135.6 nm that are observed by the GOLD mission. Please see Solomon (2017) and references therein for more details. Model codes are freely available at the HAO/NCAR website (https://www2.hao.ucar.edu).

Figure 1 compares GOLD observations with GLOW calculations for 15 December 2018 at 9 UT for both the 135.6 nm oxygen emission (O ^{5}S) and the LBH emissions. F10.7 was 72 Solar Flux Units (SFU), and Kp index was 0. For the GOLD observations, the wavelengths around the 135.6 nm spectral emission peak are summed to obtain the O ^{5}S feature brightness, while the wavelengths between 141 and 153 nm, excluding the 149.3 nm atomic nitrogen feature, are summed to find the LBH bands emission brightness. For this GLOW calculation, the atmospheric state and dynamics were modeled by TIEGCM, which was run for 15 December 2009 (solar minimum conditions) with F10.7 at 70 SFU, and all other solar indices set to low solar activity. Next the emission information was processed for the geometry of an instrument located in geostationary orbit. Lastly, the absorption by O_2 along a line of sight is included in the model calculation. The terminator is the division between night and day on the Earth, and the dawn terminator is seen on the right side of each disk image. The 15-min difference between the time of the upper disk and lower disk scans can be seen in each GOLD image, although it is more pronounced in the O ^{5}S data. There is some minor auroral activity in the Northern Hemisphere in the GOLD observations that is not seen in calculated brightnesses from GLOW for this date and time because TIEGCM was run without auroral activity inputs. Several stars can be seen in the lower left corner of the GOLD observations. The remainder of this paper examines the FUV emissions in both the model and the observations, in detail, as well as comparing them.

3. Results and Discussion

The general characteristics and evolution of the FUV emissions over a day need to be characterized in order to address more in-depth studies of the effect of waves, tides, and other phenomena. Here we address some of the calculated characteristics of O ^{5}S and LBH emissions.

Shown in Figure 2 are the GOLD observations (solid line) and GLOW calculations (dotted line) of the 135.6 oxygen emissions, O ^{5}S, for 15 December 2018 at 12 UT and 16 UT at three different row positions on the detector. The three positions on the detector roughly correspond to 23°N, the equator, and 23°S latitude. The globes on the left show the location of the data on the disk, while in the plots on the right, the *x*-axis is longitude and the *y*-axis is emission brightness (R). The GOLD observations are the average (median) of three adjacent rows on the detector. The nadir point of the satellite is at −47.5°E longitude. In the 12 UT panels the terminator is on the left side of the disk, while at 16 UT the terminator is now on the right side. At a given universal time, the longitudinal variation also corresponds to the local time variation (or solar zenith angle variation) across the disk of the Earth. This local time change with longitude can be seen in the variation in the brightness modeled and observed across the disk of the Earth. The variation of brightness as a function of longitude of the observations and model match very well. However, the magnitude of the variations in the observations and model are different. At 12 UT, the differences range from less than 10%
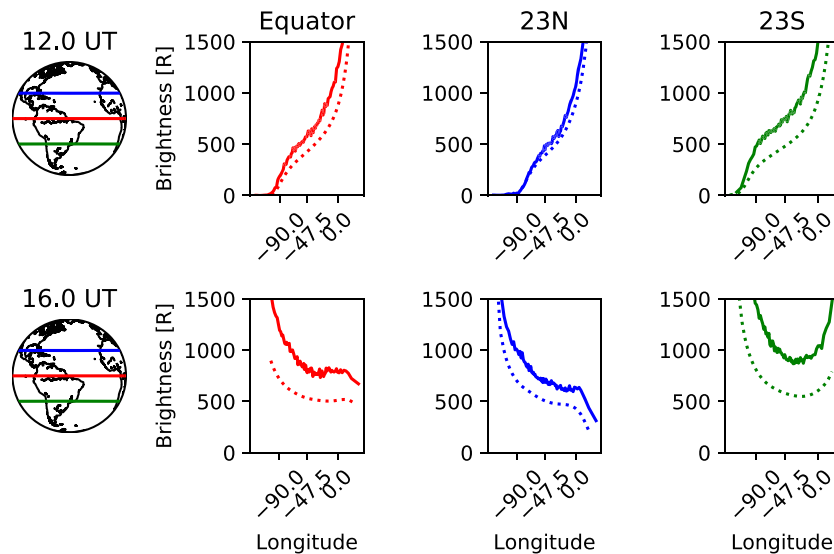
Figure 2. Panels display GOLD observations (solid line) and GLOW modeling (dotted line) for 15 December 2018 at 12 UT and 16 UT of the 135.6 oxygen emission (O ^{5}S).

to nearly 25% at the southern latitude. At 16 UT, the magnitude differences are even greater: at the equator and northern hemisphere latitude of up to 60% different and up 100% different at 23°S latitude.

There are several possible reasons for the differences between the modeled brightnesses and the GOLD observations. The modeled brightnesses depend on the composition of the atmosphere, which in turn depend on the neutral dynamics, temperatures, O_2 density, and dissociation rates of the models. The selected North and South latitudes are where the tidal effects can be significant. Disparities between the Horizontal Wind Model (HWM07, Drob et al., 2008), which drives the lower boundary of the TIEGCM in these simulations, and the actual propagating tides may have a strong effect at these latitudes. It is also known that the TIEGCM is better tuned to the real atmosphere in the northern hemisphere (Maute, 2017); this may account for some of the latitudinal difference. For the GLOW calculations, the emission cross sections for Oxygen OI 135.6 nm and the LBH band system have uncertainties as high as 30% (Meier et al., 2015; Solomon, 2017), which could also introduce a systematic bias.

Figure 3 is the same as Figure 2 but for the LBH emission; these are for again solar minimum and geomagnetically quiet conditions. The brightness drops off faster (than the 135.6 nm emission) at large solar zenith angles; this is because the LBH emission requires photoelectron impact on the nitrogen molecules. Where there is less sunlight (at higher solar zenith angles), there is less nitrogen emission. Many of the same factors that result in differences between the GLOW calculation and O ^{5}S observations also affect the LBH bands, and again, there is uncertainty in the nitrogen cross section of up to 25% (Meier et al., 2015; Solomon, 2017).

Additional factors that may influence the longitudinal and local time variability of the FUV emissions include the terminator, the limb of the Earth, tides, geomagnetic latitude, and the equatorial ionospheric anomaly (Appleton anomaly). Both the terminator and the limb have been shown in the previous figures; the dayside limb is typically brighter than at the subsolar point. As the instrument views off nadir toward the limb, the path through the atmosphere becomes longer and contains more emitters of FUV light.

Figure 4 shows the annual cycle of LBH emissions (O ^{5}S not shown) calculated by GLOW (solid line) for solar minimum, geomagnetically quiet conditions compared to the first year of GOLD observations (dotted line). Emissions at 23°N, the geographic equator, and 23°S are shown. The equator (red) has maxima at the equinoxes and minima at the solstices. The 23°N location (blue) exhibits a peak in June and a minimum in December, while the 23°S location (green) displays a maximum in January and a minimum in June. The 23°S peak is slightly stronger than the 23°N peak. The early GOLD observations are suggestive of GLOW calculations being correct in shape, if not magnitude, as explained around Figures 2 and 3.
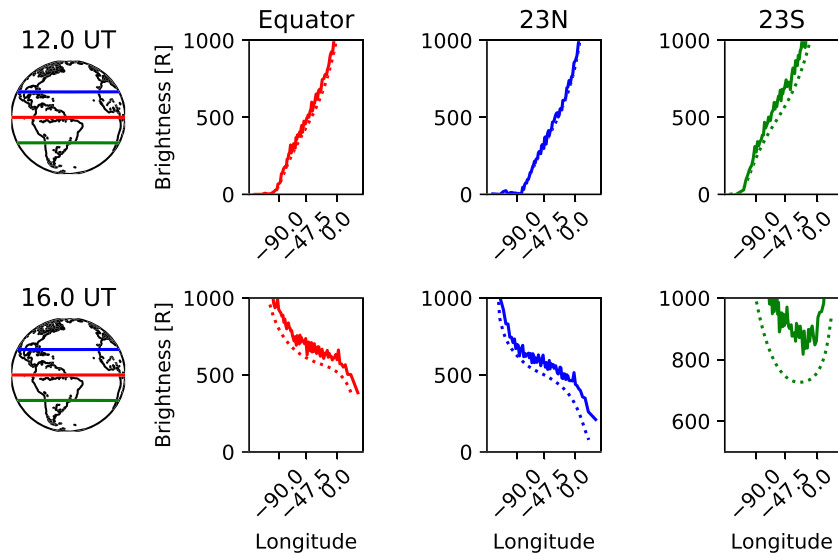
Figure 3. Panels display GOLD observations (solid lines) and GLOW modeling (dotted lines) for 15 December 2018 at 12 UT and 16 UT for the LBH band emissions.

A well-known and prominent feature seen in FUV emissions of Earth is the Equatorial Ionization Anomaly (EIA). It appears in the FUV as two crests of oxygen emission at about $\pm15°$ latitude from the geomagnetic equator. The processes that govern the development of the EIA involve the upward ExB drift of plasma near the equator (e.g., Balan et al., 2018; Lin et al., 2007) which produces the crests of ionization. Figure 5 compares the EIA simulated by TIEGCM and the nightglow emissions calculated by GLOW with observations from GOLD on 15 November 2018 at 23 UT. The O ^{5}S emission is a proxy for plasma in the EIA. The geomagnetic equator (Burrell et al., 2018) is shown as a green line. The EIA is more readily identifiable in November than on 15 December 2018 because the EIA is stronger, as is typical nearer equinox (Liu & Watanabe, 2008). At night, the EIA is seen in GOLD observations as two crests of emission that extend across the Atlantic Ocean until local times near midnight, sometimes even into the morning hours. However, while an EIA is present in GLOW calculations, it is less bright, the crests are less distinct, the symmetry between crests is lacking, and the plasma crests do not extend as far over the Atlantic. The difference between the observations and the GLOW calculations is due to the TIEGCM model that generates the EIA. That TIEGCM does not properly represent that the nighttime EIA is a known problem of the model. One possible reason that TIEGCM is not properly representing the nighttime EIA is that the model is not lofting the plasma high enough. If the plasma is not lofted high enough, it experiences recombination more quickly resulting in lower plasma densities in the EIA.

During quiet solar and geomagnetic activity conditions, tides are a strong source of variability of the thermosphere, up to 60–80% of the variability (Gasperini et al., 2015). TIEGCM's lower boundary is forced by HWM07 (Drob et al., 2008) to introduce migrating and non-migrating tides. However, by turning these tides off we can examine the impact they have on the FUV emissions of the thermosphere.

Figure 6 shows the contribution of the migrating and non-migrating (both diurnal and semi-diurnal) tides to the O ^{5}S and LBH emission brightnesses (R) and the effective temperature (K) at 12 UT and 19 UT. The effective temperature is a weighted column integrated temperature given by

$$T_{eff}(\chi, \psi) = \frac{\int_0^\infty T(s)\eta(s)ds}{B(\chi, \psi)}, \qquad (1)$$

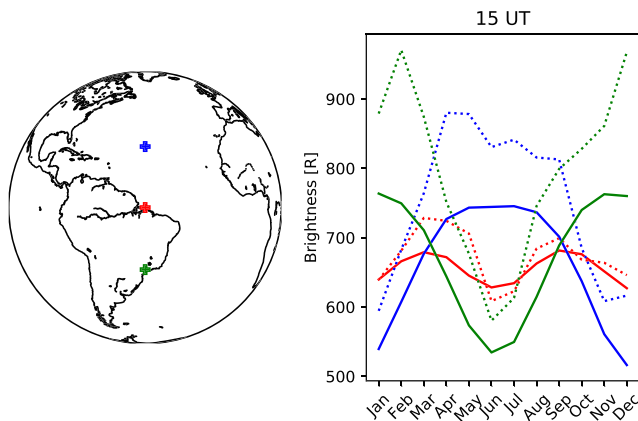where this is a function of the viewing geometry angles X and Ψ, and

Figure 4. LBH emission brightness at 15 UT throughout the year for 23°N (blue), 0°N (red), and 23°S (green). The TIEGCM model F10.7 parameter was set to 70 SFU, and Kp index was set to 0. The solid line is the model while the dotted line is early GOLD observations.
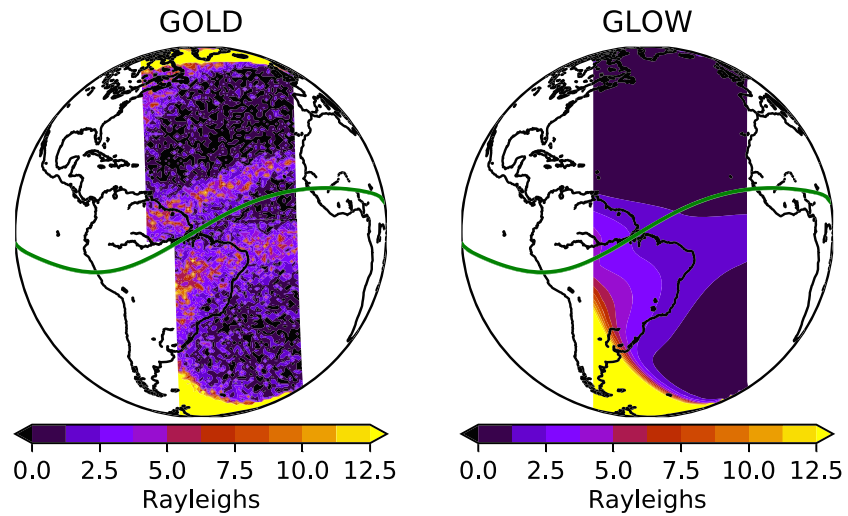
Figure 5. O ^{5}S emission signal at 23 UT showing the equatorial ionospheric anomaly (EIA) for 15 November. F10.7 was 73 SFU and Kp index was 1. The geomagnetic equator is plotted as a green line.

T(s) is temperature along the line of sight, η(s) is the emission contribution function along the line of sight, and B(X,Ψ) is the emergent brightness at a specific observation angles. T_{eff} takes into account observational geometry and any O_2 absorption. Without use of equation (1), an estimate of the effective temperature can be obtained by taking the absolute temperature at the altitude peak of the emission feature (near 155 km). This is because the temperature at this emission peak contributes the most to the weighted column integrated effective temperature.

Evident in Figure 6 is the anticorrelation of O ^{5}S and LBH emissions (see over Africa at 12 UT and the Eastern Pacific at 19 UT). This anticorrelation is expected due to differential advection of O and N_2 in the lower thermosphere (Greer et al., 2018; Hickey et al., 2015). Without the diurnal and semidiurnal migrating and non-migrating tides, up to 50 R of the O ^{5}S emission and up to 20 R of the LBH emission variability is missing. In addition, the tides induce a variability of ±50 K in the effective temperature. The structure in
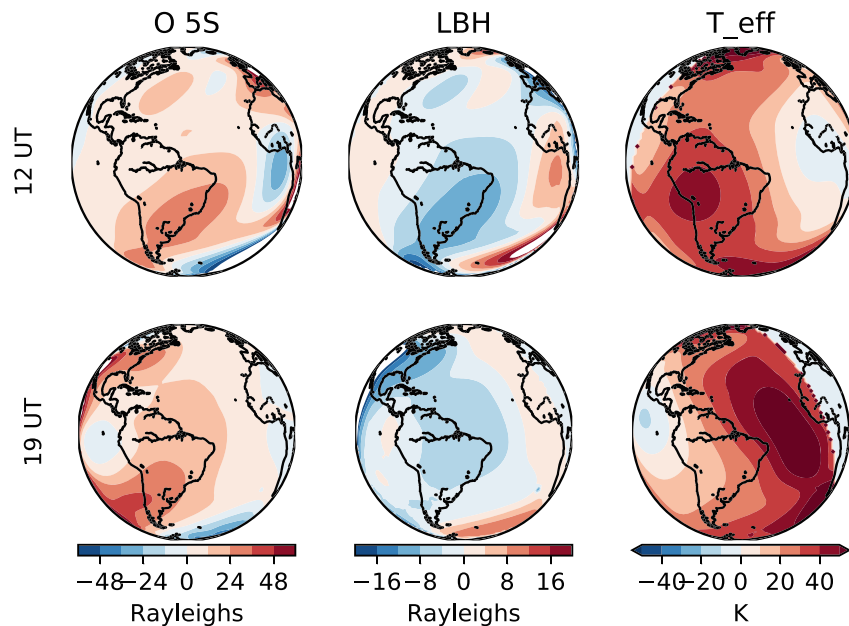

Figure 6. Contribution of migrating and non-migrating tides in TIEGCM to the O ^{5}S and LBH emission brightnesses (Rayleighs) and the effective temperature (K) at both 12 UT and 19 UT.
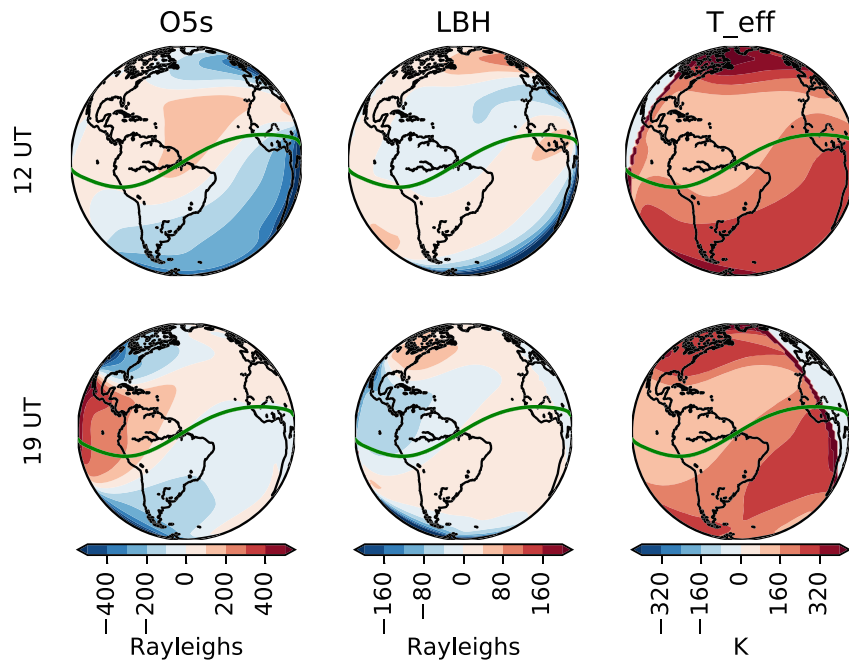
Figure 7. The change in brightnesses for the O ^{5}S and LBH emissions (Rayleighs) and the effective temperature change (K) at 12 UT and 19 UT between a geomagnetic quiet day and a geomagnetic active (Kp = 7) 15 December day. The green line is the geomagnetic equator.

T_{eff} is reminiscent of the diurnal eastward wave number 3 (DE3) tide. This tide has significant consequences for the thermosphere and ionosphere (e.g., Immel et al., 2006; Pedatella et al., 2012). Other tides that appear to be critical for this region and the FUV emissions are diurnal Westward wave number 2 (DW2), diurnal Eastward wavenumber 2 (DE2), and diurnal Westward wavenumber 5 (DW5).
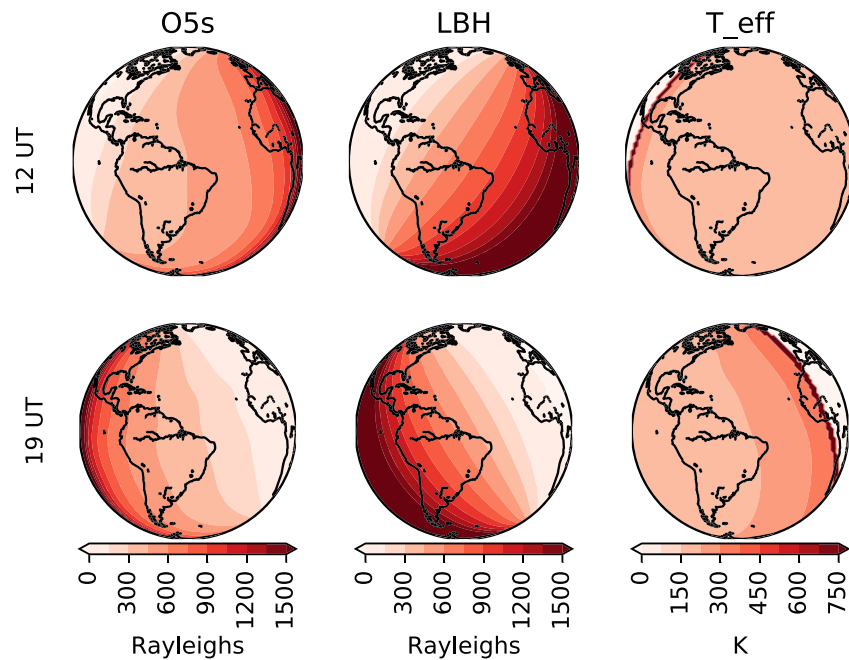

Figure 8. The change in brightnesses for the O ^{5}S emission (Rayleighs), LBH emission (Rayleighs), and the effective temperature (K) at between a solar maximum day (F10.7 = 210) and a solar minimum day (F10.7 = 70) for 15 December at 12 UT and 19 UT.

The change in brightnesses for the O ^{5}S and LBH emissions (R) and the effective temperature change (K) at 12 UT and 19 UT between a geomagnetic quiet and a geomagnetic active day (Kp = 7) at solar minimum for a 15 December day is shown in Figure 7. The effect of geomagnetic activity is some 10 times greater than that of the tides. According to models, this level of geomagnetic activity is expected to contribute a variability of greater than 800 R to the O ^{5}S signal and more than 320 R to the LBH signal. Additional energy input from the geomagnetic storm elevates the effective temperature by 300 K or more and increases the variability of the FUV emissions, especially in the high latitudes.

Figure 8 shows the spatial gradients in O ^{5}S and LBH emission and effective temperature for solar maximum conditions. The structure of the emissions across the disk is similar to solar minimum although it is nearly a kR brighter. The effective temperature of the thermosphere is also hotter, by some 250 K. The transition across the terminator is more abrupt at solar maximum. The greater gradients at the terminator may induce solar terminator waves around the June solstice (Forbes et al., 2008; Liu et al., 2009). As we move into solar maximum, we can expect a brighter disk as viewed by GOLD.

4. Conclusions

Using the models TIEGCM and GLOW, the brightness of the Earth's disk in the O ^{5}S 135.6 nm oxygen emission and the LBH band emission from geostationary orbit showed expected variability in local time, latitude, season, tides, geomagnetic activity, and solar activity. The model trends match the observations well, if not the absolute magnitude. However, the modeling failed to adequately portray the extraordinary nighttime EIA, especially its distinct crests that extend well into the low latitude nightside. The calculated brightness of the O ^{5}S emission was shown to vary by ±45 R due to tides alone. Increasing solar activity significantly increased the brightness of the disk, while increased geomagnetic activity generated brightness changes of up to ±400 R. Future observations will contribute to improving models, and eventually, forecasts of ionospheric weather anomalies impacts on communications and navigation.

References

Anger, C. D., Babey, S. K., Broadfoot, A. L., Brown, R. G., Cogger, L. L., Gattinger, R., et al. (1987). An ultraviolet auroral imager for the Viking spacecraft. *Geophysical Research Letters*, *14*(4), 387–390. https://doi.org/10.1029/GL014i004p00387

Balan, N., Souza, J., & Bailey, G. J. (2018). Recent developments in the understanding of equatorial ionization anomaly: A review. *Journal of Atmospheric and Solar-Terrestrial Physics*, *171*, 3–11, ISSN 1364-6826. https://doi.org/10.1016/j.jastp.2017.06.020

Barth, C. A., & Schaffner, S. (1970). Ogo 4 spectrometer measurements of the tropical ultraviolet airglow. *Journal of Geophysical Research*, *75*(22), 4299–4306. https://doi.org/10.1029/JA075i022p04299

Burrell, A. G., Halford, A., Klenzing, J., Stoneback, R. A., Morley, S. K., Annex, A. M., et al. (2018). Snakes on a spaceship—An overview of Python in heliophysics. *Journal of Geophysical Research: Space Physics*, *123*, 10,384–10,402. https://doi.org/10.1029/2018JA025877

Carruthers, G. R., & Page, T. (1972). Apollo 16 far-ultraviolet camera/spectrograph: Earth observations. *Science*, *177*(4051), 788–791. https://doi.org/10.1126/science.177.4051.788

Christensen, A. B., Paxton, L. J., Avery, S., Craven, J. D., Crowley, G., Humm, D. C., et al. (2003). Initial observations with the Global Ultraviolet Imager (GUVI) in the NASA TIMED satellite mission. *Journal of Geophysical Research*, *108*(A12), 1451. https://doi.org/10.1029/2003JA009918

Chubb, T. A., & Hicks, G. T. (1970). Observations of the aurora in the far ultraviolet from OGO 4. *Journal of Geophysical Research*, *75*(7), 1290–1311. https://doi.org/10.1029/JA075i007p01290

Conway, R. R., Meier, R. R., & Huffman, R. E. (1988). Satellite observations of the oi 1304, 1356 and 1641 Å dayglow and the abundance of atomic oxygen in the thermosphere. *Planetary and Space Science*, *36*(10), 963–973, ISSN 0032-0633. https://doi.org/10.1016/0032-0633(88)90034-7

Drob, D. P., Emmert, J. T., Crowley, G., Picone, J. M., Shepherd, G. G., Skinner, W., et al. (2008). An empirical model of the Earth's horizontal wind fields: HWM07. *Journal of Geophysical Research*, *113*, A12304. https://doi.org/10.1029/2008JA013668

Eastes, R. W. (2000). Modeling the N2 Lyman-Birge-Hopfield bands in the dayglow: Including radiative and collisional cascading between the singlet states. *Journal of Geophysical Research*, *105*(A8), 18,557–18,573. https://doi.org/10.1029/1999JA000378

Eastes, R. W., Feldman, P. D., Gentieu, E. P., & Christensen, A. B. (1985). The ultraviolet dayglow at solar maximum: 1. Far UV spectroscopy at 3.5 Å resolution. *Journal of Geophysical Research*, *90*(A7), 6594–6600. https://doi.org/10.1029/JA090iA07p06594

Eastes, R. W., McClintock, W. E., Burns, A. G., Anderson, D. N., Andersson, L., Codrescu, M., et al. (2017). The global-scale observations of the limb and disk (GOLD) mission. *Space Science Reviews*, *212*(1-2), 383–408. https://doi.org/10.1007/s11214-017-0392-2

Forbes, J. M., Bruinsma, S. L., Miyoshi, Y., & Fujiwara, H. (2008). A solar terminator wave in thermosphere neutral densities measured by the CHAMP satellite. *Geophysical Research Letters*, *35*, L14802. https://doi.org/10.1029/2008GL034075

Frank, L. A. (1998). Global auroral imaging for the dynamics explorer mission.

Gasperini, F., Forbes, J. M., Doornbos, E. N., & Bruinsma, S. L. (2015). Wave coupling between the lower and middle thermosphere as viewed from TIMED and GOCE. *Journal of Geophysical Research: Space Physics*, *120*, 5788–5804. https://doi.org/10.1002/2015JA021300

Greer, K. R., England, S. L., Becker, E., Rusch, D., & Eastes, R. (2018). Modeled gravity wave-like perturbations in the brightness of far ultraviolet emissions for the GOLD mission. *Journal of Geophysical Research: Space Physics*, *123*, 5821–5830. https://doi.org/10.1029/2018JA025501

Hickey, M. P., Walterscheid, R. L., & Schubert, G. (2015). A full-wave model for a binary gas thermosphere: Effects of thermal conductivity and viscosity. *Journal of Geophysical Research; Space Physics*, *120*, 3074–3083. https://doi.org/10.1002/2014JA020583

Huffman, R., LeBlanc, F., Larrabee, J., & Paulsen, D. (1980). Satellite vacuum ultraviolet airglow and auroral observations. *Journal of Geophysical Research*, *85*(A5), 2201–2215. https://doi.org/10.1029/JA085iA05p02201

Immel, T. J., Sagawa, E., England, S. L., Henderson, S. B., Hagan, M. E., Mende, S. B., et al. (2006). Control of equatorial ionospheric morphology by atmospheric tides. *Geophysical Research Letters*, *33*, L15108. https://doi.org/10.1029/2006GL026161

Knipp, D. J., Ramsay, A. C., Beard, E. D., Boright, A. L., Cade, W. B., Hewins, I. M., et al. (2016). The May 1967 great storm and radio disruption event: Extreme space weather and extraordinary responses. *Space Weather*, *14*, 614–633. https://doi.org/10.1002/2016SW001423

Lin, C. H., Hsiao, C. C., Liu, J. Y., & Liu, C. H. (2007). Longitudinal structure of the equatorial ionosphere: Time evolution of the four-peaked EIA structure. *Journal of Geophysical Research*, *112*, A12305. https://doi.org/10.1029/2007JA012455

Liu, H., Lühr, H., & Watanabe, S. (2009). A solar terminator wave in thermospheric wind and density simultaneously observed by CHAMP. *Geophysical Research Letters*, *36*, L10109. https://doi.org/10.1029/2009GL038165

Liu, H., & Watanabe, S. (2008). Seasonal variation of the longitudinal structure of the equatorial ionosphere: Does it reflect tidal influences from below? *Journal of Geophysical Research*, *113*, A08315. https://doi.org/10.1029/2008JA013027

Maute, A. (2017). Thermosphere-ionosphere-electrodynamics general circulation model for the ionospheric connection explorer: TIEGCM-ICON. *Space Science Reviews*, *212*(1-2), 523–551. https://doi.org/10.1007/s11214-017-0330-3

Meier, R. R., Picone, J. M., Drob, D., Bishop, J., Emmert, J. T., Lean, J. L., et al. (2015). Remote sensing of Earth's limb by TIMED/GUVI: Retrieval of thermospheric composition and temperature. *Earth Space Science*, *2*(1), 1–37. https://doi.org/10.1002/2014EA000035

Mende, S. B., Frey, H. U., Rider, K., Chou, C., Harris, S. E., Siegmund, O. H. W., et al. (2017). *Space Science Reviews*, *212*(1-2), 655–696. https://doi.org/10.1007/s11214-017-0386-0

Mende, S. B., Heetderks, H., Frey, H. U., Lampton, M., Geller, S. P., Habraken, S., et al. (2000). Far ultraviolet imaging from the image spacecraft: 1. System design. In J. L. Burch (Ed.), *The image mission* (244 pp.). Dordrecht: Springer. https://doi.org/10.1007/978-94-011-4233-5_8

Murphree, J. S., King, R. A., Payne, T., Smith, K., Reid, D., Adema, J., et al. (1994). The Freja ultraviolet imager. *Space Science Reviews*, *70*(3–4), 421–446. https://doi.org/10.1007/BF00756880

Nicholas, A. C., Craven, J. D., & Frank, L. A. (1997). A survey of large-scale variations in thermospheric oxygen column density with magnetic activity as inferred from observations of the FUV dayglow. *Journal of Geophysical Research*, *102*(A3), 4493–4510. https://doi.org/10.1029/96JA03464

Paxton, L. J., Morrison, D., Strickland, D. J., McHarg, M. G., Zhang, Y., Wolven, B., et al. (2003). The use of far ultraviolet remote sensing to monitor space weather. *Advances in Space Research*, *31*(4), 813–818, ISSN 0273-1177. https://doi.org/10.1016/S0273-1177(02)00886-4

Paxton, L. J., Schaefer, R. K., Zhang, Y., & Kil, H. (2017). Far ultraviolet instrument technology. *Journal of Geophysical Research: Space Physics*, *122*, 2706–2733. https://doi.org/10.1002/2016JA023578

Pedatella, N. M., Hagan, M. E., & Maute, A. (2012). The comparative importance of DE3, SE2, and SPW4 on the generation of wavenumber-4 longitude structures in the low-latitude ionosphere during September equinox. *Geophysical Research Letters*, *39*, L19108. https://doi.org/10.1029/2012GL053643

Qian, L., Burns, A. G., Emery, B. A., Foster, B., Lu, G., Maute, A., Richmond, A. D., Roble, R. G., Solomon, S. C., & Wangm, W. (2014). The NCAR TIE-GCM: A community model of the coupled thermosphere/ionosphere system. In *Modeling the Ionosphere-Thermosphere System, AGU Geophysical Monograph Series*.

Richmond, A. D., Ridley, E. C., & Roble, R. G. (1992). A thermosphere/ionosphere general circulationmodel with coupled electrodynamics. *Geophysical Research Letters*, *6*, 601–604.

Solomon, S. C.(2017). Global modeling of thermospheric airglow in the far ultraviolet. *Journal of Geophysical Research, Space Physics*, *122*, 7834–7848. https://doi.org/10.1002/2017JA024314

Strickland, D. J., Evans, J. S., & Paxton, L. J. (1995). Satellite remote sensing of thermospheric O/N2 and solar EUV: 1. Theory. *Journal of Geophysical Research*, *100*(A7), 12,217–12,226. https://doi.org/10.1029/95JA00574

Strickland, D. J., Meier, R. R., Walterscheid, R. L., Craven, J. D., Christensen, A. B., Paxton, L. J., et al. (2004). Quiet-time seasonal behavior of the thermosphere seen in the far ultraviolet dayglow. *Journal of Geophysical Research*, *109*, A01302. https://doi.org/10.1029/2003JA010220

Torr, M. R., Torr, D. G., Zukic, M., Johnson, R. B., Ajello, J., Banks, P., et al. (1995). *Space Science Reviews*, *71*(1-4), 329–383. https://doi.org/10.1007/BF00751335